IEEE Access
Multidisciplinary | Rapid Review | Open Access Journal

Received June 7, 2021, accepted June 15, 2021, date of publication June 24, 2021, date of current version July 13, 2021.

Digital Object Identifier 10.1109/ACCESS.2021.3090773

Design of an Artificial Muscle Pressure Supply Mode Based on the Connected Structure

CHENGHANG LI, LEI ZHANG, (Member, IEEE), SHUANG ZHANG, PEIQI XU, AND CHUNLI WANG

Department of Automation and Control, Ocean University of China, Qingdao 266100, China

Corresponding author: Lei Zhang (zhanglei1107@ouc.edu.cn)

ABSTRACT This paper proposes an air pressure supply structure for artificial muscles. The main body of the structure comprises a hollow tube, an electromagnet in the outer layer, and a magnetic piston in the inner diameter of the tube. At both ends, a hose interface connects the air inlet of the artificial muscle. Under the action of controlling changes in current, the electromagnet nested in the outer wall causes the movement of the piston by changing the force between the electromagnet and the magnetic piston and by changing the law of air pressure in the tube. Because the inside of the tube is a closed space, the movement of the magnetic piston in the tube causes a change in the volume of the gas at both ends, thus forming pressure differences of different sizes and directions. Therefore, this air supply, with specific oscillatory characteristics, can be used to produce the desired movement of artificial muscles. Through system modeling, theoretical analysis, and simulation experiments of the connected pressure supply structure, we verified that the system has inherent characteristics similar to a spring damping structure. In view of the inherent characteristics of this kind of structure, this paper introduces the trend of input and output changes by considering the deviation value, details how to improve the traditional neural network PID control algorithm, and discusses the intelligent optimization of controller parameters. Simulation results show that the improved control method can effectively overcome the nonlinear and coupling characteristics of the system, and the gas supply structure can provide a continuous pressure supply curve of an arbitrary waveform and a frequency within a certain amplitude range. The designed air supply structure was applied to a quadruped robot, using its oscillating characteristics to generate rhythmic movement. Compared with the traditional pressure control method, the piston was driven to produce reciprocating motion by fully exploiting the energy stored in the compressed gas, so as to reduce the external energy input and reduce the comprehensive energy consumption of the system. In addition, the control algorithm improved in this paper can meet diverse pressure requirements for driving artificial muscles. Moreover, the independent control of leg support force and stiffness can be realized by combining it with the antagonistic joints. This structure can be widely used in the pressure supply of outdoor robot artificial muscle.

INDEX TERMS Adjustable stiffness and flexibility, pneumatic artificial muscle, pressure supply structure.

I. INTRODUCTION

The pneumatic artificial muscle (PAM) has been widely studied in various fields because of its low weight, small volume, high flexibility, and good biocompatibility. Mirvakili and Hunter [1] analyzed the material, structure, and driving mechanism of artificial muscle and found that the performance indicators of artificial muscle actuators, such as force, power, cost, lifecycle, and efficiency, exceeded those of biological muscle. Yin *et al.* [2] simulated an artificial muscle calf joint model designed by a natural neuromuscular model and showed that it successfully performed over 92% of the muscle activation that was naturally made by human participants. Terryn *et al.* [3] applied the Diels–Alder polymer to artificial muscle, giving soft robots not only bionic flexibility for absorbing shock and preventing body damage but also a certain degree of self-healing ability. Park *et al.* [4] designed a wearable robot device assisting in ankle-foot rehabilitation, which utilized four PAMs to assist in dorsiflexion, flexion, inversion, and eversion, and could provide active help without limiting the freedom of the ankle joint. Das *et al.* [5] designed an interactive glove for the human wrist to assist in the movement of injured wrist joints for rehabilitation. Trivedi and Rahn [6] improved the shape detection method of a soft

The associate editor coordinating the review of this manuscript and approving it for publication was Wai-Keung Fung.

robot so that its flexible manipulator could better adapt to the environment and grasp objects of different sizes through the operation of the whole arm. Radojicic *et al.* [7] combined a PAM driver and a rubber bellow driver to achieve controllable joint stiffness and improve the safety of the system.

The traditional PAM model adopts the direct pressure supply mode based on an air compressor, which requires a large volume for the pressure supply link and high overall energy consumption. To apply PAM to a foot robot, an air compressor must be installed, which increases the load and is not always feasible. Therefore, this paper proposes an artificial muscle air pressure supply structure with a low weight, small volume, and convenient assembly. This structure is based on the principle of a communication device; it can control the air pressure of two muscles at the same time, and it can make full use of the energy stored by compressed gas to greatly reduce the comprehensive energy consumption of the system. However, the nonlinearity, multi-coupling, and time-ductility of the proposed structure make it difficult to control the air pressure.

At present, the most widely used PAM models are the Colbrunn model [8] and the Reynolds model [9]. Based on these models, Colbrunn *et al.* [10] studied aerodynamic drive characteristics and established a control model of the dynamic airflow regulated by the solenoid valve. Tagami *et al.* [11] took full account of the effect of the supply pipeline on the output air pressure and improved the response capacity of the pressure control by measuring the PAM inlet air pressure value in combination with the compensation circuit. Xie *et al.* [12] used the improved Generalized Prandtl-Ishlinskii (GPI) model to build a length-pressure hysteresis model for PAM and modified the envelope function of the operator in the model to an arctangent function, which improved the ability to capture the relationship between length and pressure hysteresis. Zhang *et al.* [13] used a Kalman filter to estimate the model error and used the estimated error for control compensation, which improved the control performance. Ba and Ahn [14] and Vo *et al.* [15] used time delay estimation to approximate the nonlinearity and perturbation in the system, and then proposed a robust sliding mode control compensator, which effectively overcame the uncertainty, unknown quality, and high nonlinearity of system dynamics. Tang *et al.* [16] improved the conventional nominal characteristic trajectory following (NCTF) controller by removing actual speed feedback and adding acceleration feedback compensators to the model. The improved NCTF controller greatly improved tracking accuracy compared with the traditional NCTF and classic PID controllers. With improvements in deep learning technology, new developments have been made in the PAM control mode. Sun and Chen *et al.* [17] comprehensively analyzed the model parameter error, external interference, and influence of the air source and proposed an online estimation system. The parameter method, combined with an adaptive algorithm [18] and output force control, could well cope with the error caused by model time variation and air pressure control lag. Zhang *et al.* [19] used the external input model implemented by the nonlinear autoregressive moving average and recursive fuzzy neural network to predict the characteristics of dynamic models with rate- and load-dependent effects. Experiments showed that the model could predict the dynamic hysteresis behavior with rate- and load-dependent effects well. Chavoshian *et al.* [20] used a particle swarm optimization algorithm to optimize PID-DNN parameters. Compared with the traditional sliding mode controller, the controller could track the reference signal more effectively under the complex environment of the PAM model. Anh *et al.* [21] proposed a new adaptive neural network control algorithm considering the influence of the internal coupling effect and the external end-effect contact force. It improved the compliance force/position output performance of a highly nonlinear tandem PAM robot. Chiang and Chen [22] proposed an intelligent adaptive control algorithm considering the compressibility of air and the elasticity of PAM materials. By adjusting the control gain of the fuzzy sliding mode controller and the integrator to minimize the tracking error, the adaptive control algorithm was realized.

The combination of artificial muscles and bionic antagonism joints has become a new trend of development as it can realize the leg flexibility and the stiffness of the independent control at the same time. Merola *et al.* [23] adopted an antagonistic artificial muscle model to establish a feedforward compensation control system for calculating torque to drive the nonlinear dynamics of the joint, and combined the Proportion Integration Differentiation (PID) control action with feedforward compensation to achieve fast and accurate tracking control performance.

Bugurlu *et al.* [24] designed a force feedback controller with stability based on the dissipative principle and derived a set of PAM input force criteria corresponding to the expected joint torque and stiffness, which realized the independent control of joint torque-stiffness and joint dislocation-stiffness. Zhang *et al.* [25] used a sliding mode controller and an equivalent spring PAM model to realize the independent control of different waveforms of torque and the stiffness of antagonistic joints.

Yu and Jian [26] designed a tracking controller for the lower extremity exoskeleton using nonlinear model predictive control (NMPC) and extended the echo state network. Xiong *et al.* [27]–[29] studied a bionic hexapod robot. They used a multi-layer neural network and an antagonistic joint model structure to realize variable stiffness and efficient walking of the robot to adapt to different ground surfaces and analyzed system energy consumption, which promoted the development of artificial muscle for practical application. Jacob *et al.* [30] used Artificial Muscle Intelligence with Deep Learning (AMIDL) systems to translate user intent captured by electroencephalogram (EEG) sensors into artificial muscle movements to help paralyzed patients express their thoughts and feelings.

The development of science and technology and the expansion of application fields [31]–[35] have resulted in higher requirements for the leg flexibility and support force control

of foot robots. A connected structure has not only the characteristics of nonlinearity and coupling, like the PAM model, but also oscillation of the special features, which means the system control accuracy is associated with the expected signal characteristics and time delay. Therefore, an adaptive neural network PID control algorithm is proposed in this paper. The expected signal and the vibration state are introduced as system input so that the pressure tracking effect is in good agreement. The idea presented in [24] was used to decouple the antagonistic bionic joint, and the control algorithm presented in this paper was used to study the practical application of the pressure supply structure. Compared with the traditional air compressor pressure supply mode, the pressure supply mode and control algorithm proposed in this paper have the following characteristics:

1. Low weight, small volume, and ease of carrying. Compared with the pneumatic servo valve, the structure proposed in this paper does not need to be equipped with other complex structures; the equipment structure is simple, the volume is small, and it can be better carried on outdoor equipment.
2. It can make full use of the energy stored in compressed gas and can greatly reduce the comprehensive energy consumption of the system. In the process of motion, the energy stored when gas is compressed pushes the piston to do a round-trip motion, which reduces the input of external energy in subsequent motion.
3. The pressure supply curve is continuous. In practical application, to ensure the stability and low vibration of the body, the output force of artificial muscle is limited and continuous, and has no obvious step. The air pressure curve generated by the structure is realized by the movement of the piston. This ensures the continuity of the pressure supply curve in principle, and there is no need to use other methods to limit the jumping of the pressure curve.
4. The PID controller based on input and feedback can realize the adaptive adjustment of parameters and improve the robustness and reliability of the system. The introduction of piston position and its motion state can produce good prediction ability for model parameters and controller output.

The rest of this paper is organized as follows. In section II, the proposed gas supply structure is modeled, its dynamic characteristics and the influence of each model parameter on the characteristics are analyzed in detail, and the design method of the model parameters is given. Section III introduces in detail the design process of the pressure control method based on this model. Section IV details the simulation of the pressure control effect of a single structure to verify the control precision of the model. Based on the bionic antagonistic joint structure of the leg robot, the pressure supply method and control algorithm proposed in this paper were used to simulate the torque and stiffness control effect to verify the application prospect of the model. Finally, Section V summarizes the contents of the paper and the application prospects of the proposed algorithm in the field.

II. STRUCTURAL DESIGN AND MODELING

In this section, the model structure and the air–force relationship formed inside the structure are analyzed and modeled. Then, the dynamics model of the piston is deduced by force analysis of the whole structure. Finally, the influences of each structural parameter on the inherent characteristics of the model are simulated and analyzed, and the method to select the model parameters according to the actual application is given.

A. CONNECTOR STRUCTURAL DESIGN

The structure consists of a circular tube with a smooth inner wall and a magnetic piston embedded in it. The tube is fitted with hoses at both ends to connect the air inlet of the artificial muscle, creating an enclosed space inside the structure. In the process of moving in the tube, the piston is driven by pressure difference owing to the change in gas volume at both ends. Combined with the gait of the foot robot, the piston can make full use of the expansion energy of compressed gas.

The electromagnet embedded in the outer wall of the tube can affect the movement of the piston in the tube by changing the input current so as to adjust the air pressure supplied by the artificial muscle. Its structural model is shown in Fig. 1.

Assuming that the displacement of the piston at the middle position is 0, the motion is positive to one side and negative to the other side. The gas volumes at both ends of the pipe are as follows when the piston is located at x:

$$\begin{aligned} V_l &= V_{l0} + sx, \\ V_r &= V_{r0} - sx, \end{aligned} \tag{1}$$

where V_l and V_r are the volumes of the round tubes at the left and right ends of the piston, respectively; V_{l0} and V_{r0} are the volumes of the containers at the left and right ends, respectively, when the piston is at zero, and $V_{l0} \approx V_{r0}$; S is the area of the piston; and $x$is the displacement of the piston.

According to the ideal gas state equation,

$$pV = nrT_{emp}, \tag{2}$$

where p is the gas pressure in Pa; V is the gas volume in m^3; n is the number of moles of a gas, in mol; T is the system temperature, in K; and r is the gas constant (proportionality constant), in J/(mol·K). For a mixture of gases, such as air, the pressure, p, is a linear combination of the partial pressures of the components. Therefore, (2) can be written as follows:

$$pV_{\text{air}} = n_{\text{air}} r T_{emp}. \tag{3}$$

Combining (1) and (3),

$$\begin{aligned} p_l &= \frac{n_{\text{airl}} r T_{emp}}{V_{l0} + sx} = \frac{k_l(T_{emp})}{V_{l0} + sx}, \\ p_r &= \frac{n_{\text{airr}} r T_{emp}}{V_{r0} - sx} = \frac{k_r(T_{emp})}{V_{r0} - sx}. \end{aligned} \tag{4}$$

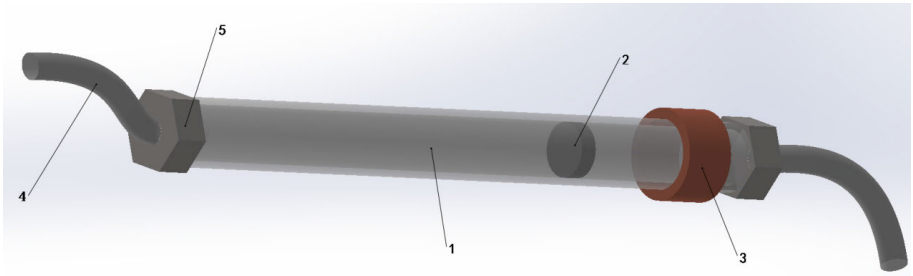

1. Center round pipe 2. Magnetic piston 3. Electromagnet 4. Air guide hose 5. Connecting wire cap

FIGURE 1. Gas connectivity structure diagram.

In (4), $K_l(T) = n_{airl}rT$, where n_{airl} is the quantity of air at the left end of the container, which is a constant that does not change with displacement when the container is encapsulated. The same is true at the right end. Additionally, p_l and p_r represent the gas pressure at the left and right ends of the piston, respectively, and are functions of displacement,x, external temperature, T, and muscle expansion. In the same scene, the working environment temperature of muscle usually does not change dramatically, so it can be regarded as a constant in simulation. Here, the expansion of muscle refers to a slight change in the volume of gas in the central circular tube caused by the change in the shape of the artificial muscle caused by the expansion of muscle. As its influence on the change in the volume of gas in the central circular tube is small, it can be ignored.

Equation (5) gives the relationship between the pressure and the pressure of the mixed gas:

$$F = ps. \tag{5}$$

Substituting the above equation into (4), we get

$$\begin{aligned} f_l &= \frac{k_l(T_{emp})}{V_{l0} + sx}s, \\ f_r &= \frac{k_r(T_{emp})}{V_{r0} - sx}s, \end{aligned} \tag{6}$$

where f_l and f_r are the forces exerted on the piston by the air pressure at the left and right ends of the piston, respectively. The resultant force is the gas pressure applied to the piston at displacement x.

$$f = f_r - f_l. \tag{7}$$

B. STRESS ANALYSIS

In the horizontal direction of the model, the piston is acted on by four forces: pressures, f_l and f_r; dynamic friction,f_f; and magnetic attraction, f_G, from both sides of the gas. The force analysis of the piston is shown in Fig. 2.

$$\begin{cases} f - f_f - f_G = ma \\ \ddot{x} = a \\ x_{t=0} = x_0 \\ \dot{x}_{t=0} = 0 \end{cases} \tag{8}$$

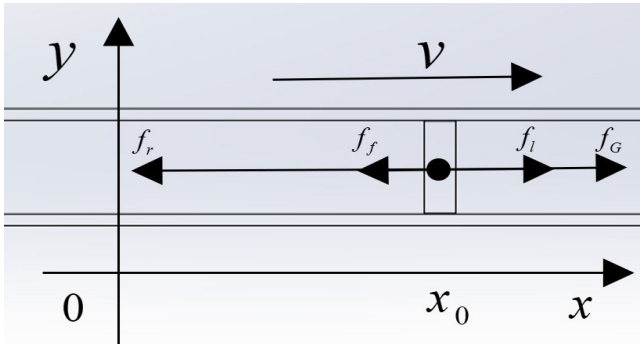

FIGURE 2. Force analysis of the piston.

Rearranging (8) gives us

$$x = x_0 + \frac{1}{m}\int_0^t \int_0^t \left(\frac{k_r(T_{emp})}{V_{r0} - sx}s - \frac{k_l(T_{emp})}{V_{l0} + sx}s - f_f - f_G\right)dtdt. \tag{9}$$

In the formula, f_f is the dynamic friction force, which is related to the material and manufacturing process. In application, by properly reducing the contact force between the piston and the pipe wall and the shape of the piston, such as the similar bullet-shaped structure at both ends, lengthening the transverse dimension of the piston, and filling the gap of the contact surface with liquid lubricant, the friction and air leakage of the system could be reduced to a range with less impact on the system. Dynamic friction, f_f, is the constant in this experiment; x_0 is the initial position of the piston, the velocity is zero at this point; and m is the mass of the piston. According to [36]–[38], the electromagnetic attraction of a DC solenoid can be expressed as follows:

$$f_G = \frac{N^2U^2\mu_0 S}{2R^2K_f^2(x_d - x)^2}, \tag{10}$$

where N is the number of coil turns; U is the input voltage at both ends of the electromagnet; μ_0 is the vacuum permeability, and its value is $0.04\pi(Wb/(A \cdot m))$; S is the cross-sectional area of the magnetic circuit; R is the winding resistance; K_f is the magnetic flux leakage coefficient, which is affected by magnetic circuit composition and material; and x_d is the installation position of the electromagnet.

Let the fixed parameter in the model be $K_c = \frac{N^2\mu_0 S}{2R^2K_f^2}$. Equation (10) can be simplified as follows:

$$f_G = K_c \frac{U^2}{(x_d - x)^2}. \tag{11}$$

C. ANALYSIS OF INHERENT CHARACTERISTICS

The mass of the piston is limited to 200 g, the length of the connected structure is 15 cm, and the cross-sectional area is 0.16π cm^2. The force change and movement trajectory of the piston in the connected structure when the initial state of the piston is given as $x_0 = 10$ cm and $v_0 = 0$ are shown in Fig. 2. The initial gas pressure, p, is $10^4 Pa$. Different initial pressure designs affect the range of the output pressure of the structure, which is determined by the expected output force of the muscles in practical application and the selected parameters of the PAM model.

The force changes and movement trajectories of the piston in the connected structure are shown in Fig. 3.

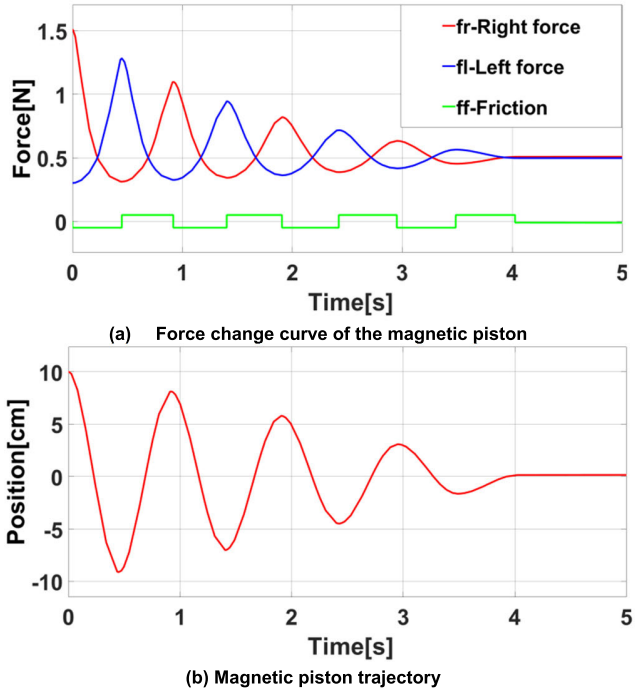

FIGURE 3. Connected structure characteristics at zero input.

At the initial time, the piston is at the right end of the center point. At this time, the total volume of gas at the right end of the piston is small, and the pressure change caused by each movement displacement, Δx, is great. As the piston moves to the left of the center point, the total volume of gas at the right side of the piston increases, thereby reducing the rate of change in pressure at the right side. Under the action of friction, the gas thrust, f_r, at the right end of the piston shows a U-shaped attenuation trend, and the thrust, f_l, at the left end is the same, as shown in Fig. 3(a).

At the initial time, the initial position,x, of the piston is adjusted by the pre-input of the external magnet $x_0 \neq 0$. At this time, the gas pressure at the right end of the piston is greater than that at the left end, and the sum of the left end thrust, f_l, and the friction force received by the piston in the connected structure is less than the right end thrust, f_r. The piston makes a quasi-sinusoidal oscillation motion with amplitude attenuation in the connected structure, as shown in Fig. 3(b). Under zero input, the motion of the structure is caused by the compressed gas energy storage in the non-zero initial state. The number of piston motion cycles is related to the friction force of the system and the initial potential energy of the piston.

The main model parameters that affect the period of internal pressure change are piston mass, tube length, cross-sectional area, and the initial position of piston.

The control variable method was used to simulate the influence of the shock characteristics under the main model parameters. The simulation parameters in each figure are listed in Table 1, and the corresponding simulation results are shown in Fig. 4(a)–(d).

TABLE 1. Simulation parameter table.

Structure parameter name	Correspondence analysis diagram			
	Fig. 4(a)	Fig. 4(b)	Fig. 4(c)	Fig. 4(d)
Piston mass (g)	–	200	200	200
Round tube length (cm)	15	–	15	15
Initial position (cm)	10	10	–	10
Cross-sectional area (cm^2)	0.16π	0.16π	0.16π	–

In Fig. 4(a), the influence of piston mass on the structural inherent pressure change is analyzed. The piston mass is taken as 100 g, 200 g, and 500 g, and other model parameters are shown in Table 1. The lower the piston mass, the smaller the oscillation cycle. This is because a smaller piston mass produces a larger acceleration, which speeds up the oscillation of the piston, and at the same time, under the same force of friction, the fast oscillation speed also increases the power done by friction and makes the system reach a stable point more quickly.

Under different connected structure pipe lengths but other model parameters fixed, as shown in Table 1, the characteristics of pressure change, as shown in Fig. 4(b). When the initial position stays the same, the increase in pipe length reduces the gas pressure on both ends around the initial position of the piston. The combined force applied to the piston is reduced, thereby reducing the acceleration and velocity of the piston motion and increasing the natural oscillation period of the piston. A shorter pipe length accelerates the friction power and gives the piston more potential energy at the initial time, which makes the frequency faster and the movement time longer.

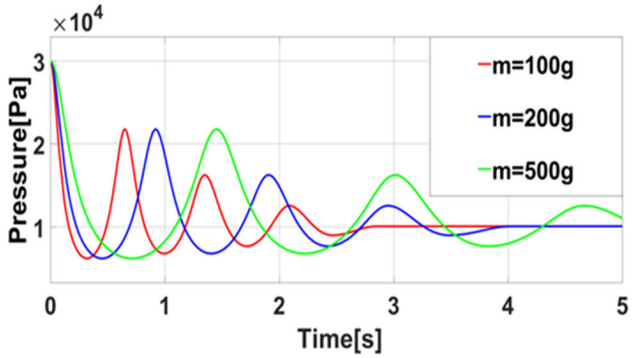

(a) Influence of piston mass on oscillation period

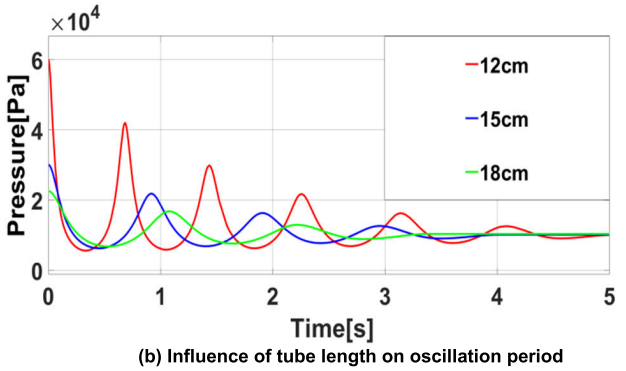

(b) Influence of tube length on oscillation period

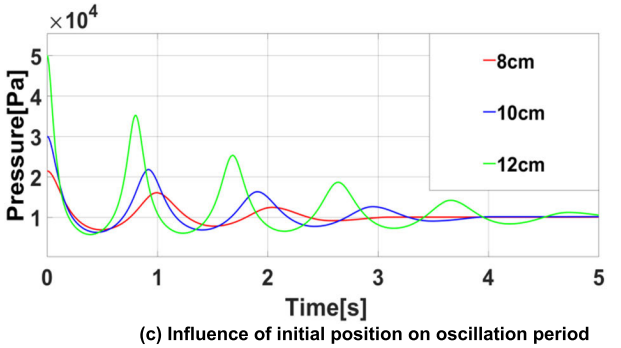

(c) Influence of initial position on oscillation period

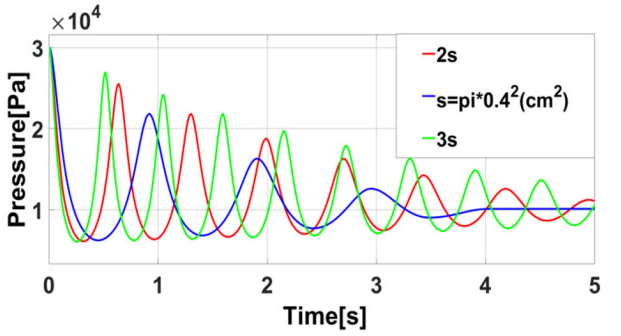

(d) Influence of cross-sectional area of circular tube on oscillation period

FIGURE 4. Influence of model parameters on the natural oscillation characteristics of the piston.

Under different initial positions of the piston but other model parameters fixed, as shown in Table 1, the characteristics of pressure also change, as shown in Fig. 4(c). The piston has greater potential energy under the larger initial position. The piston's impact on the oscillation characteristics is similar in principle to that of shortening the length of the round tube at the same position.

Finally, the influence of pipe cross-sectional area on pressure was analyzed with the fixed model parameters, as shown in Table 1. The simulation results are shown in Fig. 4(d). As the pipe cross-sectional area increases, owing to the condition of invariable length, the total volume of the structure increases, which reduces the proportion of the gas volume to the artificial muscle volume, so the initial pressure in the pipe increases slightly. Therefore, it can be seen that in the model, the volume of gas in the artificial muscle and the gas in the connecting hose in the total gas volume of the connected structure have a partial influence on the piston oscillation characteristics, and the influence is related to the proportion of gas. At the same time, the increased cross-sectional area of the pipe increases the pressure on the piston under the same pressure, which accelerates the oscillation frequency and increases the initial potential energy of the piston.

In summary, the oscillation frequency of the piston is negatively correlated with the piston mass and the length of the pipe, and positively correlated with the initial position of the piston and the cross-sectional area (radius) of the pipe. The stabilization time is related to the initial potential energy and the work consumption rate. The larger piston mass reduces the initial acceleration of the piston, the oscillation velocity of the air pressure is smaller, and the friction power is smaller. At the same time, the larger mass also increases the initial potential energy of the piston, and the stability time is longer. The influences of the length of the pipe, the initial position of the piston, and the cross-sectional area (radius) of the pipe on the oscillation period are mainly realized by changing the force in the piston motion, and the increase in force can not only accelerate the oscillation frequency but also increase the stability time.

To further analyze the coupling relationship between the natural period and the model parameters, the initial position was fixed, and the relationship between the structural radius, the length of the pipe, and the piston mass under different natural periods, T, was mapped, as shown in Fig. 5. The model parameters were limited to $m \in [10, 50]\, g$, $l \in [12, 112] cm$, and $r \in [0.2, 5.2] g$.

The point on the bottom plane in the figure is not considered because the radius of the circular tube $r \leq 0.2$ cm is beyond the limited range. The surface in the figure is the set composed of different model parameters under the same oscillation period. Under the given expected period, the appropriate model parameters can be selected in the corresponding period set according to the requirements of pipe length, piston mass, pipe diameter, and other parameters in practical application.

Assuming that the expected natural period T = 1 s is set, the coupling relationship between piston mass, tube length, and tube radius is shown in Fig. 5(b). According to the size of the robot, the suitable length of the tube $l = 15$ cm is selected. To reduce the impact of friction on the acceleration

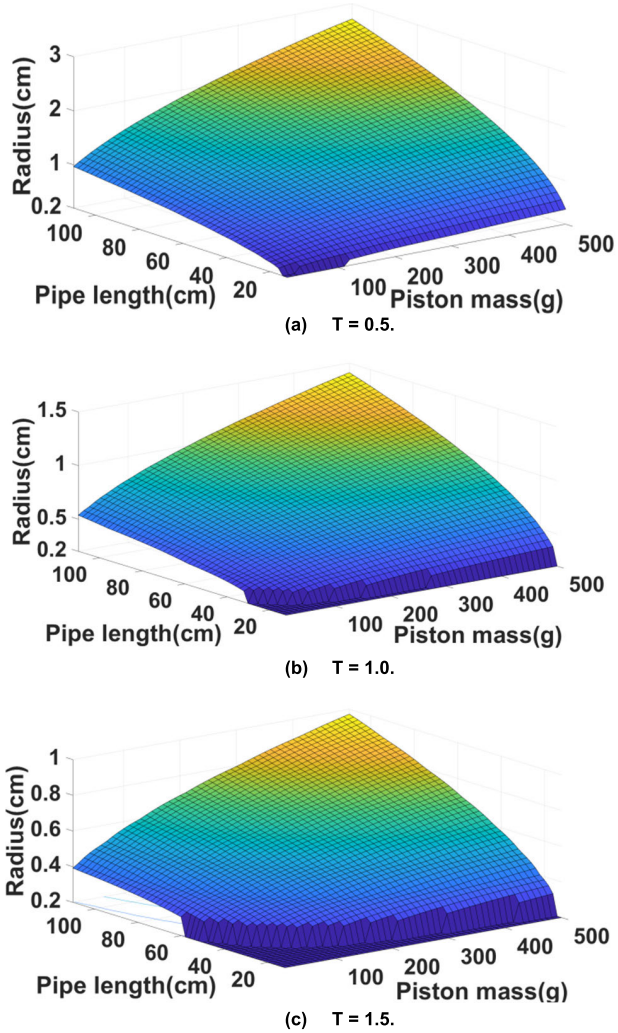

FIGURE 5. Periods and model parameter diagrams when $x_0 = 0.8l$.

of the piston, the mass of the piston should be increased appropriately. However, in practical application, the length of the piston should not be too long. In combination with the coupling relationship between piston mass and radius in the figure, the piston mass $m = 300$ g and the radius of the pipe $r = 0.16\pi$ cm^2 are selected here.

III. NEURAL NETWORK PID CONTROL ALGORITHM

The structure proposed in this paper has the following main characteristics:

A. STABILITY CHARACTERISTICS OF THE SYSTEM

First, from the structural model, when the piston is close to a certain point (such as the right end point), the gas pressure on the right side of the piston increases rapidly, which prevents the piston from moving to the right. Second, the piston is affected by friction in the process of motion, and the amplitude of the piston decreases continuously in the process of motion.

The model motion equations (6) and (9) also show this characteristic; when it is close to the right end point $(V_{r0}-\mathrm{sx}) \to 0$, that is, the gas volume at the right end of piston is close to 0, the piston is greatly pushed to the left by air pressure $f_l \to \infty$. Therefore, the initial parameters of the controller do not affect the stability of the system.

B. THE MAIN FACTORS OF THE MODEL ARE LESS

From (9), it can be seen that, assuming that the operating environment temperature of the system does not change dramatically, the parameters affecting the system model are a controlled quantity, and there are no other time-varying factors.

Input and feedback based on a neural network PID controller has certain adaptability to time-varying systems and greatly reduces the demand of the accuracy of the model. However, the traditional error-based PID controller only considers the relative error between input and output and its trend. It cannot fully reflect the influence of the inherent oscillation characteristics in the structure proposed in this paper on the output of the controller.

According to the difference between the natural pressure oscillation trend and the expected pressure movement trend of the connected structure at the control time, the control states can be divided into three categories, as shown in Table 2.

TABLE 2. Control state classification table.

Change trend	sp increase	sp keep	sp reduce
pv increase	c^-	c	c^+
pv keep	c	c	c
pv reduce	c^+	c	c^-

In Table 2, sp is the expected pressure value, pv is the inherent pressure change trend of the system at the set time, c^+ means that the output value of the controller demand should increase compared with the traditional PID control, c means that it should increase to a lesser degree, and c^- means that it should be reduced appropriately. When the motion states of sp and pv are opposite of c^+, to enable the output air pressure of the connecting structure to better track the expected value, in addition to the thrust generated by the gas in the pipe received by the piston, the inertial force in the original movement direction of the piston needs to be overcome. Compared with the result calculated by the pure relative error, the controller needs a larger output force. When the two motion states are in the same state as c^-, the piston motion direction is consistent with the expected direction, and the controller output only needs to change the speed of the piston motion, which requires less output force compared with the other two states.

It can be seen that in this article, in addition to the position deviation, the factors that affect the output of the controller

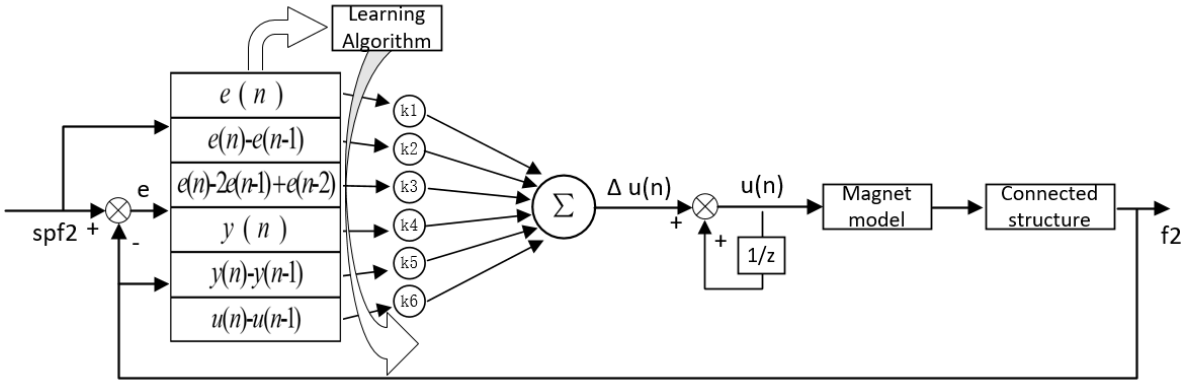

FIGURE 6. Neural network PID control block diagram.

include the initial state of the desired curve and the respective movement trends of *sp* and *pv*. However, the PID controller based on the deviation design alone cannot reflect the influence of the respective movement states. According to the specific characteristics of this structure, three parameters are introduced to the PID controller on the basis of the previous object control: the output control object, the first order differential of the output control object, and the first order differential of the expected signal. The overall control block diagram is shown in Fig. 6.

The output increment of the controller is $\Delta u(n) = KX^T$, where K is the parameter matrix to be optimized, and X is the input matrix of neural network, so

$$\begin{cases} K = [k_1, k_2, k_3, k_4, k_5, k_6] \\ X = \begin{bmatrix} e(n) \\ e(n) - e(n-1) \\ e(n) - 2e(n-1) + e(n-2) \\ y(n) \\ y(n) - y(n-1) \\ u(n) - u(n-1) \end{bmatrix}^T \end{cases}. \tag{12}$$

Then, the output of the controller is as follows:

$$u(n) = u(n-1) + \Delta u(n). \tag{13}$$

Set the total control object model as $y = \psi(\mathrm{u})$; then,

$$y(n) = \psi(u(n)). \tag{14}$$

The objective function of training is as follows:

$$J = \frac{1}{2}(r(n) - y(n))^2. \tag{15}$$

Use the gradient descent method to optimize parameter K:

$$\begin{cases} \Delta k_i = \eta e(n) \dfrac{\partial \psi(u(n))}{\partial u(n)} x_i \\ k(n+1) = k(n) + \Delta k_i. \end{cases} \tag{16}$$

In this paper, as the control object is not easy to find, $\frac{\partial \psi(u(n))}{\partial u(n)}$ is replaced with $\frac{\psi(u(n)) - \psi(u(n-1))}{u(n) - u(n-1)}$. The error can be reduced by adjusting the η value.

The core goal of the controller is to provide the voltage supply structure with any waveform and continuous voltage supply curves in a certain amplitude range. The improved control method has the following characteristics:

1. The controller reduces the requirement of system accuracy based on input and feedback.
2. The best linear combination is found from the complex PID three-parameter combinations by using the adaptive property of neural network, and the automatic real-time adjustment of parameters can be realized, which can effectively improve the robustness and reliability of the system.
3. The introduction of piston position and its motion state can produce good prediction ability for model parameters and controller output.

IV. SIMULATION AND EXPERIMENT

A. NETWORK TRAINING

It can be seen from III that the controller has six inputs and six outputs. The goal of training is to initially find the relationship between different combinations of input states and outputs. The basic training process is as follows:

1. Determine the initial parameters of the controller.

First, after the model parameters are selected, the pressure difference between the left and right ends of the piston is estimated according to the expected maximum supply pressure $|f_r - f_l|$, and its maximum $|f_r - f_l|_{\max}$ appears at the end of the design motion interval.

At t_0, $u(n-1) = 0$, let $\Delta u(n) = |f_r - f_l|_{\max}$, so that the output has only the gain term k_1, then $k_1 = \frac{\Delta u(n)}{x_0}$, and we initialize $k_3 = k_2 = 0.1\ k_1,$, $k_4 = k_5 = k_6 = 0$.

In the simulation model designed in this paper, the expected maximum air pressure is $10^5 p_a$. Then, there is $|f_r - f_l|_{\max} \approx 4N$, $k_1 \approx 50$.

2. The training set samples are generated and trained.

The input state of the controller is determined by the expected input curve state of the system $u(n)$, $\ddot{u}(n)$, and $\dot{u}(n)$, and the feedback state of the system $y(n)$, $\ddot{y}(n)$, and $\dot{y}(n)$.

In the continuous input state, the feedback state of the system is a follow-up, so in the training process, we only need to change the state of the input curve at random time, and we

can generate the required samples with a large amount of data. Considering that the regulation process needs a certain time, the change frequency of input curve should not be too fast.

In this paper, changing the frequency, amplitude, and phase of the sine wave from time to time is used as the data input. The average change period of waveform is about 1 s. Combined with the feedback state of the system, the training data set is formed.

3. After a long period of data training, the training results are set as the initial parameters of the controller.

B. TRACKING RESULTS IN DIFFERENT STATES

To reduce impact to the body and the resulting energy loss, robots usually require muscles to control the continuous change of air pressure, which not only protects body parts from damage but also facilitates the smooth adjustment of the fuselage. On this basis, we carried out simulation experiments on the expected air pressure of different frequencies, phases, and waveforms. The simulation model parameters are shown in Table 3, and the simulation results are shown in Figs. 7–9. Figs. 7–9 show the control results of the neural network PID algorithm on the connected structure in the control process.

TABLE 3. Model structure parameter table.

Connected structural parameter	Size	Magnet model parameter	Size
Piston quality (m)	200 g	Number of turns in coil (N)	4000
Pipe length (l)	15 cm	Coil resistance (R)	40 Ω
Initial position (x_0)	0	Magnetic flux leakage coefficient (K_l)	2
Cross-sectional area (s)	0.16π cm^2	Installation position (x_d)	15 cm

In the zero state, the initial state of the expected pressure is set to $\varphi_0 = -0.5\pi$, $\omega_0 = 1$. When $t = 2.5\pi$, the expected frequency is changed twice as much as the original and is shown as Reference in Fig. 7(a). Under the control strategy proposed in this paper, the control results are shown as Actual in Fig. 7(a). The control error is shown in Fig. 7(b). In the initial stage, owing to the deviation between the expected pressure curve and the natural pressure oscillation curve, a large control error is generated. After the controller adjustment tends to be stable, and when the expected frequency is changed, because the position and velocity are continuous before or after the expected pressure change, the controller consumes less energy compared with the initial stage of control. The closer the expected frequency to the natural frequency of the structure, the smaller the controller output. In particular, when the expected frequency is consistent with the natural frequency, the controller output is only used to compensate for system energy consumption after reaching the expected frequency.

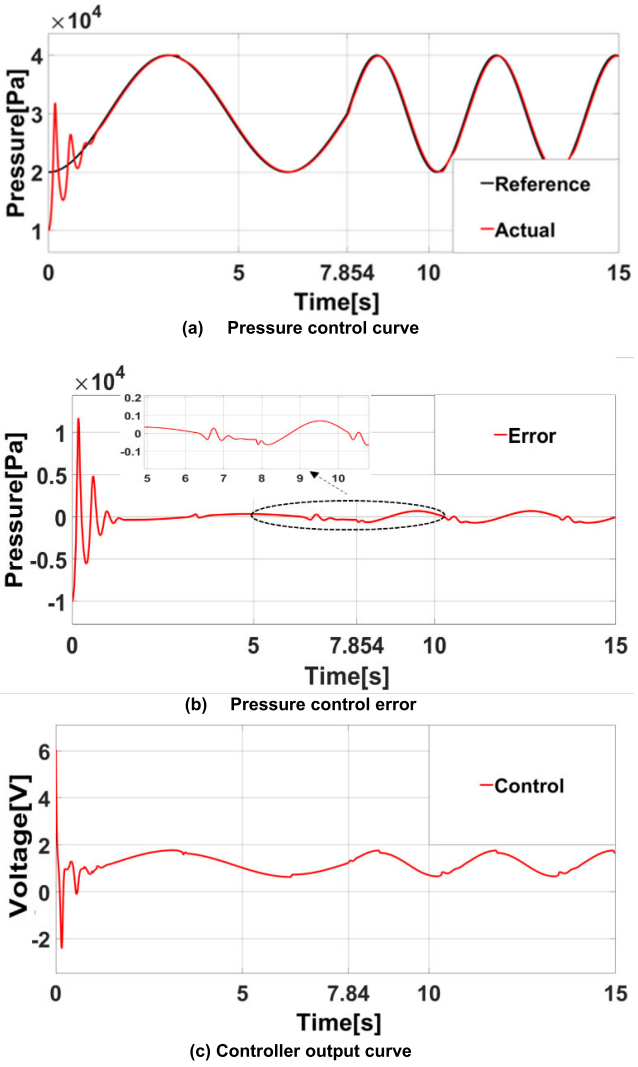

FIGURE 7. Control characteristics of different frequencies.

In Fig. 8, the initial phase $\varphi_0 = 0$ is changed. Compared with Fig. 7(b), in Fig. 8(b), the air pressure control curve has a large deviation in the initial stage of control; compared with Fig. 7(c), in Fig. 8(c), the controller output has also increased significantly at this time. This is because the initial state of Fig. 7 is consistent with the initial state of the device's inherent oscillation characteristics, which makes the switching between the two relatively smooth. Therefore, selecting an appropriate adjustment time node for adjustment can greatly reduce energy consumption and make adjustment more stable. After stabilization, the phase difference has no obvious effect on the energy consumption of the controller.

Next, we simulated the triangular wave expectation curve and changed the frequency at $t = 8$, as shown in Fig. 9. Based on the output of the controller, except at the initial stage of control and the time when the expected frequency changes, the expected curve of triangular wave needs a large output to change its motion characteristics in every half cycle.

In the stationary stage, besides compensating for system energy consumption, the controller still needs to provide a

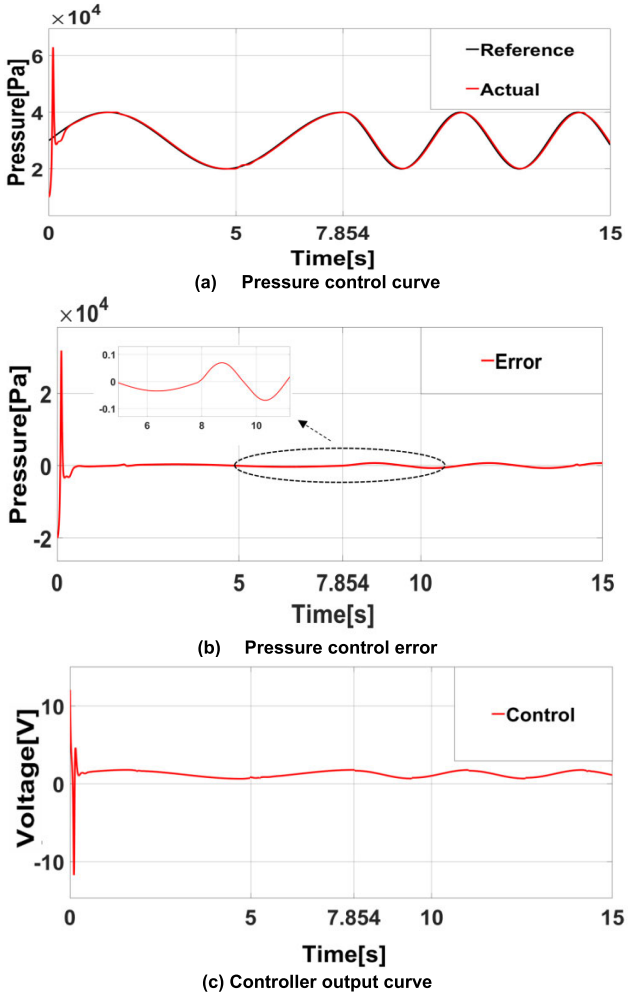

FIGURE 8. Control characteristics with different phases.

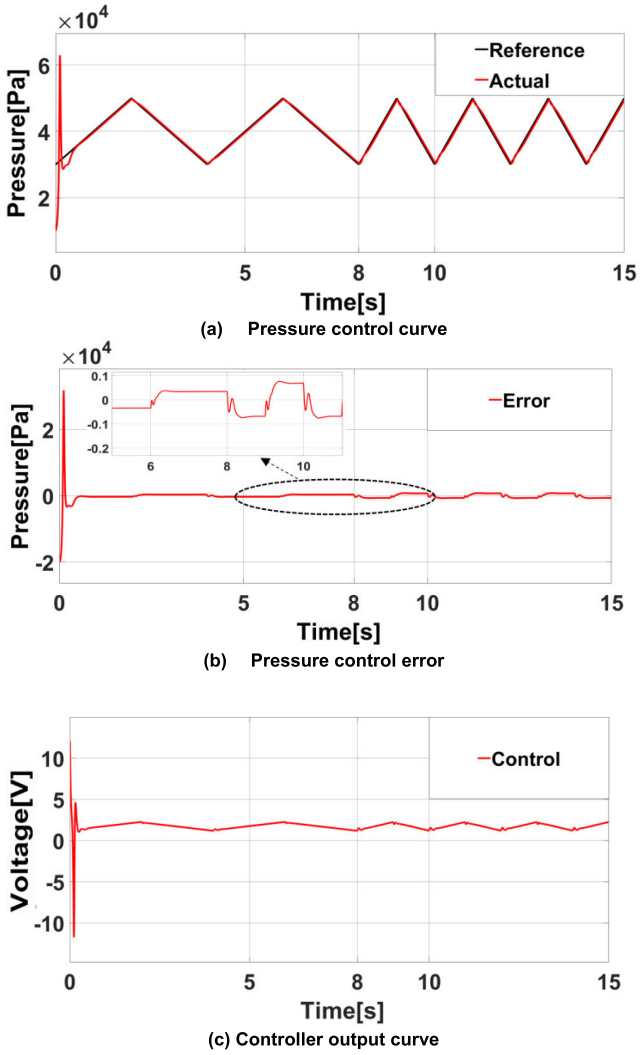

FIGURE 9. Input control characteristics of triangular wave.

small amount of energy to change the original sinusoidal characteristics. From the overall control results, the expected curve of the sinusoidal characteristics is better than that of the other curves, which is related to the inherent characteristics of the structure.

It can be seen from the figure above that the deviation of the air pressure control curve at the initial control stage is greater than that at other times. There is a large deviation between the initial expected air pressure curve and the natural air pressure oscillation curve. However, the adjustment of the controller parameters needs a process. At $t = 7.854s$, the expected curve frequency changes again, and the control error only has a small fluctuation. The controller parameters have a good adjustment process for this model. In addition, in the stable time, the small fluctuation of simulation error is caused by the change of motion direction and friction.

It can be seen from the output curves of each controller that the output of the controller is large at the early stage of control because of the difference between the natural oscillation frequency of the connected structure and the expected oscillation frequency. After a short adjustment, the system motion characteristics reach the expected value, and the controller output only needs to maintain the system energy loss. In the simulation model, the main source of loss is the friction work between the piston and the pipe. In an actual movement process, the energy stored after the gas compression in this structure will be used to push the piston to move back and forth so as to reduce the external energy input required in the subsequent movement. Therefore, the energy stored in compressed gas can be fully utilized to reduce the comprehensive energy consumption of the system.

C. INDEPENDENT CONTROL RESULTS OF STIFFNESS AND FORCE

Combined with the antagonistic bionic joint model [25], we adopted the experiment of a two-DOF quadruped robot, and the leg structure of the robot is shown in Fig. 10. The joint close to the body can swing back or forth and control the running direction and speed of the robot. As this joint is unrelated to the body shock absorption, there is no need to control its stiffness [27]. The traditional steering gear control mode was adopted for this joint. The second degree of

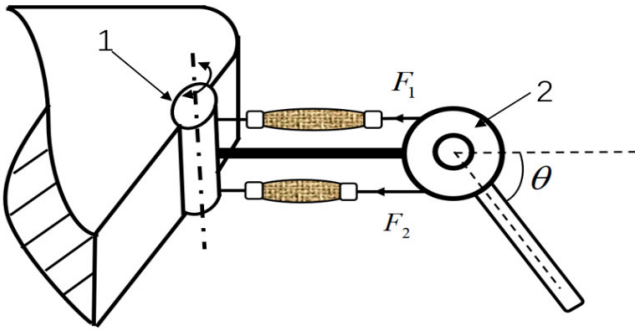

FIGURE 10. Leg structure of the robot.

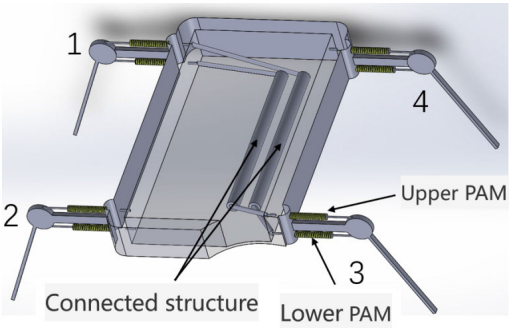

FIGURE 11. Overall connection diagram of robot.

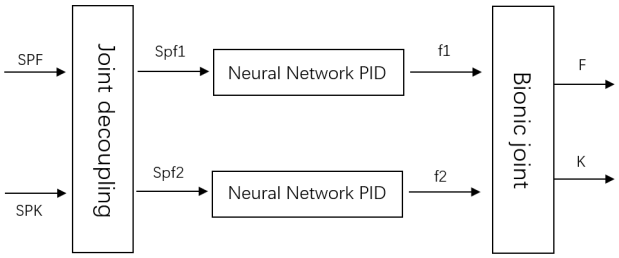

FIGURE 12. Overall control block diagram.

freedom controls the lifting and falling of the leg, which mainly affects the posture and vibration of the body. Controlling the stiffness and force of the robot can effectively improve the motion stability of the robot. The joint is driven by artificial muscle bionics and the air pressure supply structure proposed in this paper.

In this paper, a new artificial muscle is proposed to separately control the stiffness and force of legs. Combined with the movement cycle, the vibration characteristics of the air pressure are rationally used to control the input air pressure of the artificial muscles in order to reduce the energy loss of the robot. The overall connection mode is shown in Fig. 11. Because the gaits of the diagonal legs of the multi-legged robot are mostly the same, the gas connection structure between the muscles was adopted by the diagonal misjoint method. That is, the upper artificial muscle of leg 1 is connected to the lower artificial muscle of leg 3, and the lower artificial muscle of leg 1 is connected to the upper artificial muscle of leg 3. According to the symmetry principle of joint and connected structure, the movement modes of legs 1 and 3 are consistent, and the movement modes of legs 2 and 4 are consistent, which is in line with the movement characteristics of quadruped robots in a diagonal trot.

In practical application, the rotation range of a leg joint, angle θ, is between 0° and 90°. In this paper, the model of antagonistic joint driving muscle is selected as DMSP-40-120N-RM-CM, and the bionic joint radius is $R = 1$ cm. According to the three-element modeling method proposed by Zhang *et al.* [13], a PAM bionic joint model can be simplified as

$$\begin{aligned} F_1 &= [K_{11}(P_1) + K_{12}(P_1)(-x_{\mathrm{m}})](x_{m0} - x_m) \\ F_2 &= [K_{21}(P_2) + K_{22}(P_2)(x_m)](x_{m0} + x_m) \qquad (17) \\ K &= [K_{11}(P_1) + K_{12}(P_1)(-x_m)] \\ &\quad + [K_{21}(P_2) + K_{22}(P_2)(x_m)]. \qquad (18) \end{aligned}$$

In the above formulas, F, K are the preset force and stiffness, respectively; x_{m0} is the initial length of the artificial muscle in the equilibrium state; x_m is the contraction amount of the artificial muscle; P_1 and P_2 are the air supply pressures of the upper and lower artificial muscles, respectively; $K_{11}(P_1)$, $K_{12}(P_1)$, $K_{21}(P_2)$, and $K_{22}(P_2)$ are polynomial coefficients that change with pressure; and F_1 and F_2 are forces that antagonize the tension of the two artificial muscles in the upper and lower joints.

Antagonistic joints lead to a coupling relationship among the force, stiffness, and displacement of the leg, and independent control can only be achieved between any two of the three parameters [24]. In practical application, to ensure the stability and sustainable work of the body, the three parameters should meet the following requirements:

1) The force, stiffness, and displacement curves should be continuous.
2) The displacement should return to the origin after the completion of a change period, and the maximum change of displacement should not exceed $R\theta_{max}$, where R is the radius of the joint, and θ_{max} is the maximum rotatable angle of the joint.

On this basis, we first set the joint angular displacement and stiffness and used the coupling relationship to solve the corresponding size of the supporting force. According to the decoupling method proposed in [24], the tensile force required by the upper and lower artificial muscles to achieve the target stiffness and force is reversed:

$$\begin{cases} F_1 = (K - \dfrac{F + K(x_{m0} - x_m)}{2x_{m0}})(x_{m0} - x_m) \\ F_2 = \dfrac{F + K(x_{m0} - x_m)}{2x_{m0}}(x_{m0} + x_m). \end{cases} \qquad (19)$$

The core purpose of inner loop control is to ensure that accurate and stable air pressure is supplied to artificial muscles. In this paper, the muscle drive adopts the proposed air supply structure, and a neural network PID control algorithm is designed to control the input air pressure of the upper and lower muscles and to realize the stable tracking of the expected output force. Finally, through the PAM bionic joint

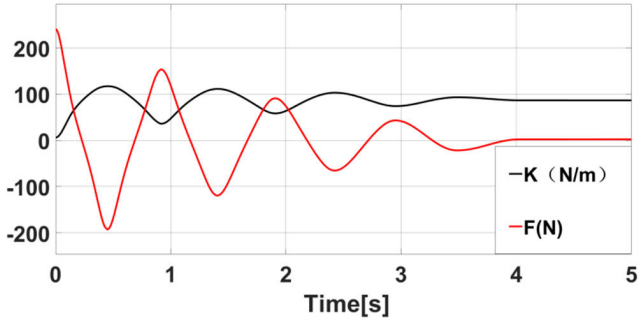

FIGURE 13. Variation curves of stiffness and force of antagonistic joints under zero input.

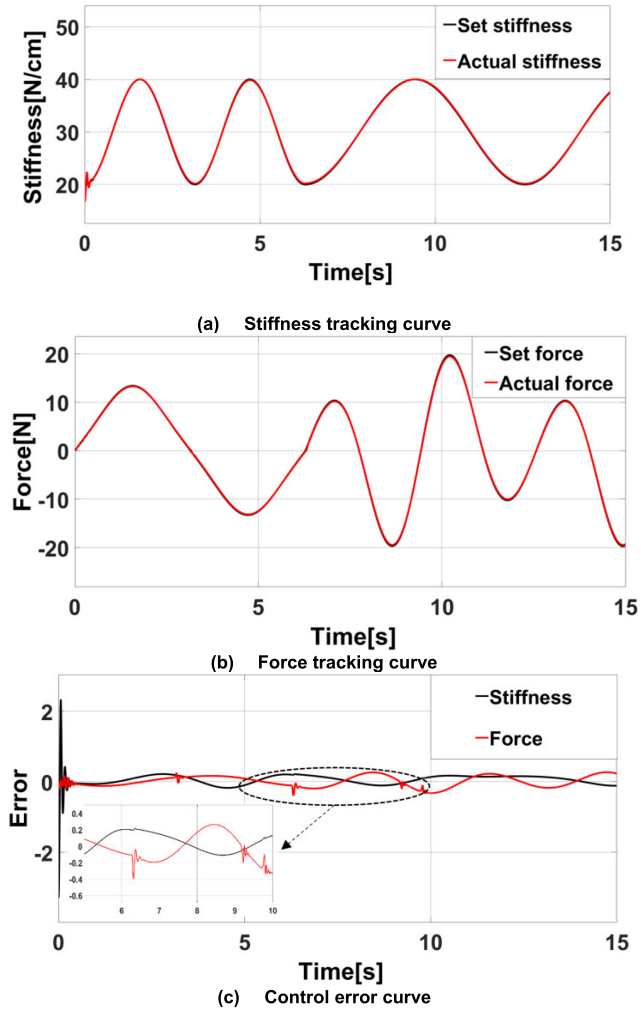

FIGURE 14. Tracking results of different stiffness and force frequency.

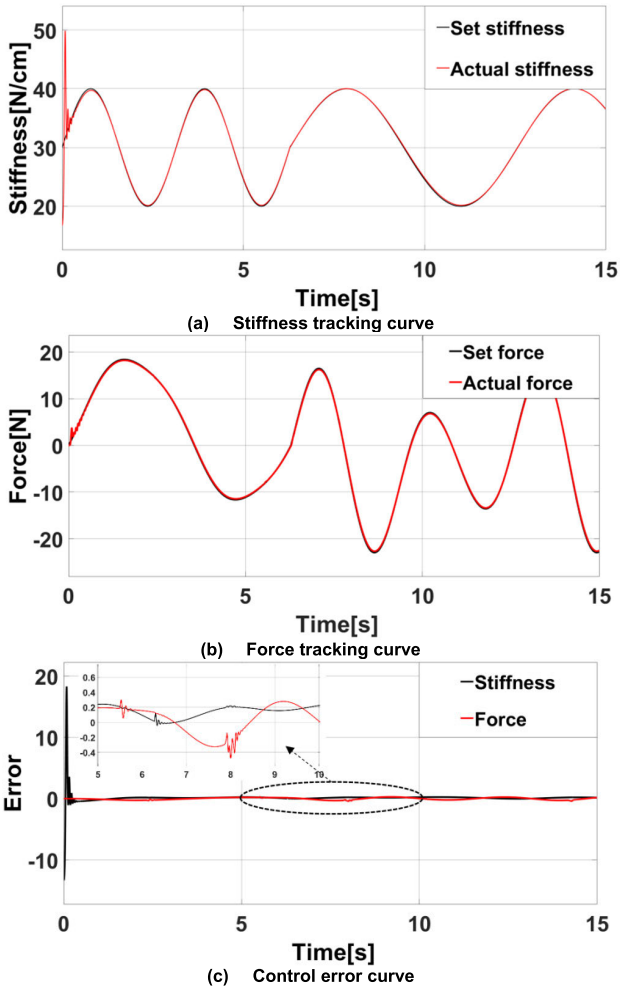

FIGURE 15. Tracking results of different stiffness and force phase.

model, the independent control effect of the expected force and stiffness is realized. The overall control block diagram is shown in Fig. 12.

The change curves of the stiffness and force of the antagonistic joint under zero input are shown in Fig. 13, and the tracking effects under various expected curves of stiffness and force are shown in Figs. 14–16.

Under the state of zero input and given a certain initial state, the supporting force of the bionic joint shows a sinusoidal motion of attenuation under the antagonistic action of two pneumatic muscles owing to the existence of the air pressure oscillation characteristic in the structure. By comparing the stiffness and supporting force curves, it is not difficult to see that when the joint compressive force increases, the antagonistic strength of the joint decreases, and the joint stiffness value decreases; otherwise, it is negative.

Figs. 14–16 show that the stiffness and force fluctuate greatly in the initial stage of control, which is related to the tracking error of the expected pressure curve in the initial stage of control. After a short adjustment, the error is limited in a small range. The air pressure control error at the initial stage of control has a small impact on the expected stiffness and force control. After the controller is stable, the control model can track the expected stiffness and force curves of different waveforms, frequencies, and phases. When the load of the robot increases, for this paper, it will affect the shape of the artificial muscle. However, the amount of gas in the structure is much larger than the variation; that is, $v_0 + sx \gg \Delta v$. Therefore, the change in the load and external interference force within the allowable range will not have a negligible impact on the performance of the design. Therefore, this

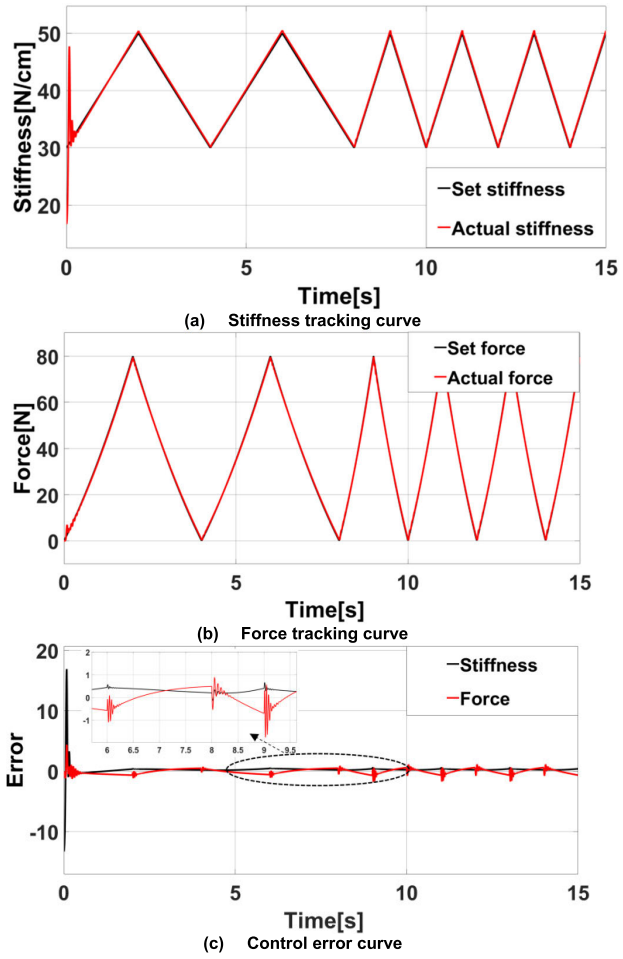

FIGURE 16. Triangle wave input tracking effect.

model can replace the traditional gas supply mode in most cases.

V. CONCLUSION

In this work, a new connected artificial muscle pressure control structure is presented, a neural network PID control algorithm is proposed according to the new air supply structure, and the expected curves of different frequencies, phases, and waveforms were tested. The experimental results indicate that

1) The connected artificial muscle pressure control structure proposed in this paper can effectively utilize the expansion energy of compressed gas and greatly reduce the energy consumption of the gas supply.
2) Under the neural network PID control algorithm, the gas supply structure can produce any pressure change curve to meet the demand, which verifies that the gas supply structure can effectively replace the traditional gas supply mode in practical application and has universality.
3) Selecting appropriate regulation nodes can effectively reduce system energy consumption and make regulation more stable. In the case of low demand, the system performance can be maximized by fully considering the inherent oscillation characteristics of the system.

The air supply structure proposed in this paper has the characteristics of light weight, low energy consumption and portable belt. Experiments show that the air supply structure can realize the independent control of joint torque and stiffness, and can replace the traditional air supply mode in most occasions. It has a wide application prospect in the application field of outdoor foot robot. In the existing antagonistic joint model, it is difficult to achieve the mutual independence of the supporting force, stiffness, and displacement of the joint leg by pulling the upper and lower artificial muscles (i.e., it is impossible to achieve the mutual independence of three outputs through two inputs). New breakthroughs in joint models are needed to make robots more flexible.

ACKNOWLEDGMENT

The authors would like to thank LetPub (www.letpub.com) for its linguistic assistance during the preparation of this manuscript.

REFERENCES

[1] S. M. Mirvakili and I. W. Hunter, "Artificial muscles: Mechanisms, applications, and challenges," *Adv. Mater.*, vol. 30, no. 6, Dec. 2017, Art. no. 1704407, doi: 10.1002/adma.201704407.
[2] K. Yin, J. Chen, K. Xiang, M. Pang, B. Tang, J. Li, and L. Yang, "Artificial human balance control by calf muscle activation modelling," *IEEE Access*, vol. 8, pp. 86732–86744, 2020, doi: 10.1109/ACCESS.2020.2992567.
[3] S. Terryn, J. Brancart, D. Lefeber, G. V. Assche, and B. Vanderborght, "Self-healing soft pneumatic robots," *Sci. Robot.*, vol. 2, no. 9, Aug. 2017, Art. no. eaan4268, doi: 10.1126/scirobotics.aan4268.
[4] Y. L. Park, B. R. Chen, N. O. Pérez-Arancibia, D. Young, L. Stirling, R. J. Wood, E. C. Goldfield, and R. Nagpal, "Design and control of a bio-inspired soft wearable robotic device for ankle-foot rehabilitation," *Bioinspiration Biomimetics*, vol. 9, no. 2, Jan. 2014, Art. no. 016007, doi: 10.1088/1748-3182/9/1/016007.
[5] S. Das, Y. Kishishita, T. Tsuji, C. Lowell, K. Ogawa, and Y. Kurita, "Wearable force-feedback glove with pneumatic artificial muscles (PAMs)," *IEEE Robot. Autom. Lett.*, vol. 3, no. 3, pp. 2416–2423, Jul. 2018, doi: 10.1109/LRA.2018.2813403.
[6] D. Trivedi and C. D. Rahn, "Model-based shape estimation for soft robotic manipulators: The planar case," *J. Mech. Robot.*, vol. 6, no. 2, May 2014, Art. no. 021005, doi: 10.1115/1.4026338.
[7] J. Radojicic, D. Surdilovic, and G. Schreck, "Modular hybrid robots for safe human-robot interaction," *Int. J. Comput. Intell.*, vol. 1, no. 6, p. 60, Dec. 2011, doi: 10.1109/SSRR.2007.4381273.
[8] R. W. Colbrunn, G. M. Nelson, and R. D. Quinn, "Modeling of braided pneumatic actuators for robotic control," in *Proc. IEEE/RSJ Int. Conf. Intell. Robots Syst. Expanding Societal Role Robot. Next Millennium*, Maui, HI, USA, Oct. 2001, pp. 1964–1970.
[9] D. B. Reynolds, D. W. Repperger, C. A. Phillips, and G. Bandry, "Modeling the dynamic characteristics of pneumatic muscle," *Ann. Biomed. Eng.*, vol. 31, no. 3, pp. 310–317, Mar. 2003, doi: 10.1114/1.1554921.
[10] L. D. Noble, R. W. Colbrunn, D.-G. Lee, A. J. van den Bogert, and B. L. Davis, "Design and validation of a general purpose robotic testing system for musculoskeletal applications," *J. Biomechanical Eng.*, vol. 132, no. 2, Feb. 2010, Art. no. 025001, doi: 10.1115/1.4000851.
[11] T. Tagami, T. Miyazaki, T. Kawase, T. Kanno, and K. Kawashima, "Pressure control of a pneumatic artificial muscle including pneumatic circuit model," *IEEE Access*, vol. 8, pp. 60526–60538, 2020, doi: 10.1109/ACCESS.2020.2983602.
[12] S. Xie, H. Liu, and Y. Wang, "A method for the length-pressure hysteresis modeling of pneumatic artificial muscles," *Sci. China Technol. Sci.*, vol. 63, no. 5, pp. 829–837, May 2020, doi: 10.1007/s11431-019-9554-y.
[13] D. Zhang, X. Zhao, and J. Han, "Active model-based control for pneumatic artificial muscle," *IEEE Trans. Ind. Electron.*, vol. 64, no. 2, pp. 1686–1695, Feb. 2017, doi: 10.1109/TIE.2016.2606080.
[14] D. X. Ba and K. K. Ahn, "A robust time-delay nonlinear controller for a pneumatic artificial muscle," *Int. J. Precis. Eng. Manuf.*, vol. 19, no. 1, pp. 23–30, Jan. 2018, doi: 10.1007/s12541-018-0003-5.

[15] C. P. Vo, X. D. To, and K. K. Ahn, "A novel adaptive gain integral terminal sliding mode control scheme of a pneumatic artificial muscle system with time-delay estimation," *IEEE Access*, vol. 7, pp. 141133–141143, 2019, doi: 10.1109/ACCESS.2019.2944197.
[16] T. F. Tang, S.-H. Chong, R. M. Nor, and K. Sato, "Practical control strategy for positioning control of pneumatic artificial muscles driven stage: Improved NCTF control," *IEEE Access*, vol. 7, pp. 85513–85524, 2019, doi: 10.1109/ACCESS.2019.2922383.
[17] N. Sun, D. Liang, Y. Wu, Y. Chen, Y. Qin, and Y. Fang, "Adaptive control for pneumatic artificial muscle systems with parametric uncertainties and unidirectional input constraints," *IEEE Trans. Ind. Informat.*, vol. 16, no. 2, pp. 969–979, Feb. 2020, doi: 10.1109/TII.2019.2923715.
[18] Y. Chen, N. Sun, D. Liang, Y. Qin, and Y. Fang, "A neuroadaptive control method for pneumatic artificial muscle systems with hardware experiments," *Mech. Syst. Signal Process.*, vol. 146, no. 1, Jan. 2021, Art. no. 106976, doi: 10.1016/j.ymssp.2020.106976.
[19] Y. Zhang, H. Liu, T. Ma, L. Hao, and Z. Li, "A comprehensive dynamic model for pneumatic artificial muscles considering different input frequencies and mechanical loads," *Mech. Syst. Signal Process.*, vol. 148, Feb. 2021, Art. no. 107133, doi: 10.1016/j.ymssp.2020.107133.
[20] M. Chavoshian, M. Taghizadeh, and M. Mazare, "Hybrid dynamic neural network and PID control of pneumatic artificial muscle using the PSO algorithm," *Int. J. Autom. Comput.*, vol. 17, no. 3, pp. 428–438, Sep. 2019, doi: 10.1007/s11633-019-1196-5.
[21] H. P. Huy Anh, N. N. Son, and C. Van Kien, "Adaptive neural compliant force-position control of serial PAM robot," *J. Intell. Robotic Syst.*, vol. 89, nos. 3–4, pp. 351–369, Mar. 2018, doi: 10.1007/s10846-017-0570-1.
[22] C.-J. Chiang and Y.-C. Chen, "Neural network fuzzy sliding mode control of pneumatic muscle actuators," *Eng. Appl. Artif. Intell.*, vol. 65, pp. 68–86, Oct. 2017, doi: 10.1016/j.engappai.2017.06.021.
[23] A. Merola, D. Colacino, C. Cosentino, and F. Amato, "Model-based tracking control design, implementation of embedded digital controller and testing of a biomechatronic device for robotic rehabilitation," *Mechatronics*, vol. 52, pp. 70–77, Jun. 2018, doi: 10.1016/j.mechatronics.2018.04.006.
[24] B. Ugurlu, P. Forni, C. Doppmann, E. Sariyildiz, and J. Morimoto, "Stable control of force, position, and stiffness for robot joints powered via pneumatic muscles," *IEEE Trans. Ind. Informat.*, vol. 15, no. 12, pp. 6270–6279, Dec. 2019, doi: 10.1109/TII.2019.2916228.
[25] D. H. Zhang, X. G. Zhao, J. D. Han, H. Y. Ma, and B. Zhang, "Independent force and stiffness control for antagonistic joint driven by pneumatic artificial muscles," *Jiqiren/Robot.*, vol. 40, no. 5, pp. 587–596, Sep. 2018, doi: 10.13973/j.cnki.robot.180256.
[26] Y. Cao and J. Huang, "Neural-network-based nonlinear model predictive tracking control of a pneumatic muscle actuator-driven exoskeleton," *IEEE/CAA J. Automatica Sinica*, vol. 7, no. 6, pp. 1478–1488, Nov. 2020, doi: 10.1109/JAS.2020.1003351.
[27] X. Xiong, F. Worgotter, and P. Manoonpong, "Adaptive and energy efficient walking in a hexapod robot under neuromechanical control and sensorimotor learning," *IEEE Trans. Cybern.*, vol. 46, no. 11, pp. 2521–2534, Nov. 2016, doi: 10.1109/TCYB.2015.2479237.
[28] X. Xiong, F. Wörgötter, and P. Manoonpong, "Neuromechanical control for hexapedal robot walking on challenging surfaces and surface classification," *Robot. Auto. Syst.*, vol. 62, no. 12, pp. 1777–1789, Dec. 2014, doi: 10.1016/j.robot.2014.07.008.
[29] X. Xiong, F. Wörgötter, and P. Manoonpong, "Virtual agonist-antagonist mechanisms produce biological muscle-like functions," *Ind. Robot: Int. J.*, vol. 41, no. 4, pp. 340–346, Jun. 2014, doi: 10.1108/IR-11-2013-421.
[30] S. Jacob, V. G. Menon, F. Al-Turjman, V. P. G., and L. Mostarda, "Artificial muscle intelligence system with deep learning for post-stroke assistance and rehabilitation," *IEEE Access*, vol. 7, pp. 133463–133473, 2019, doi: 10.1109/ACCESS.2019.2941491.
[31] G. Zhang, S. Ma, Y. Shen, and Y. Li, "A motion planning approach for nonprehensile manipulation and locomotion tasks of a legged robot," *IEEE Trans. Robot.*, vol. 36, no. 3, pp. 855–874, Jun. 2020, doi: 10.1109/TRO.2019.2961049.
[32] J. Carpentier and N. Mansard, "Multicontact locomotion of legged robots," *IEEE Trans. Robot.*, vol. 34, no. 6, pp. 1441–1460, Dec. 2018, doi: 10.1109/TRO.2018.2862902.
[33] G. Picardi, C. Laschi, and M. Calisti, "Model-based open loop control of a multigait legged underwater robot," *Mechatronics*, vol. 55, pp. 162–170, Nov. 2018, doi: 10.1016/j.mechatronics.2018.09.006.
[34] S. Li, J. Li, and Y. Mo, "Piezoelectric multimode vibration control for stiffened plate using ADRC-based acceleration compensation," *IEEE Trans. Ind. Electron.*, vol. 61, no. 12, pp. 6892–6902, Dec. 2014, doi: 10.1109/TIE.2014.2317141.
[35] Z. Li, B. Huang, Z. Ye, M. Deng, and C. Yang, "Physical human–robot interaction of a robotic exoskeleton by admittance control," *IEEE Trans. Ind. Electron.*, vol. 65, no. 12, pp. 9614–9624, Dec. 2018, doi: 10.1109/TIE.2018.2821649.
[36] L. L. Lou and H. Z. Wang, "Engineering calculation method of electromagnetic force in solenoid valve design," *Missile Space Vehicle Technol.*, vol. 1, pp. 43–48, Jan. 2007, doi: 10.3969/j.issn.1004-7182.2007.01.010.
[37] G. Tao, H. Y. Chen, and Z. B. He, "Optimal design on the magnetic field of the high-speed response solenoid valve," in *Proc. Int. Conf. Manuf. Eng. Manage.*, Xiamen, China, Oct. 2002, pp. 160–161.
[38] J. L. Qian, "Discussion on the formula of electromagnet attraction," *Elect. Eng. Technol.*, vol. 1, pp. 59–60, Jan. 2001, doi: 10.3969/j.issn.1672-9560.2001.01.026.

CHENGHANG LI received the bachelor's degree from North China Electric Power University, in 2017. He is currently pursuing the degree with the Ocean University of China. He worked in industrial boiler intelligent control systems. He competed in smart car races like Freescale Semiconductor. His research interests include robotics technology and intelligent systems.

LEI ZHANG (Member, IEEE) received the master's degree from Okayama University, Japan, in 2001, and the Ph.D. degree from Ibaraki University, in 2006. He is currently a Lecturer with the School of Engineering, Ocean University of China. His research interests include robotics and bionic robot and its control.

SHUANG ZHANG received the bachelor's degree in engineering, in 2019. She is currently pursuing the master's degree in control engineering with the Ocean University of China. Her research interests include low-energy consumption posture and intelligent system of hexapod robots.

PEIQI XU received the bachelor's degree in automation from the Ocean University of China, in 2019, where she is currently pursuing the master's degree in control engineering. Her main research interests include attitude control and motion control of hexapod robot.

CHUNLI WANG was born in Shandong, China, in 1997. She received the bachelor's degree in measurement and control technology and instrumentation from Qingdao Agricultural University, in 2019. She is currently pursuing the master's degree in control engineering with the Ocean University of China. Her research interests include the research and control of intelligent instruments and the research on terrain adaptability of hexapod robots.